Crystal-crystal phase transformation via surface-induced virtual premelting

Valery I. Levitas,[1,*] Zhaohui Ren,[2] Yuewu Zeng,[2,3] Ze Zhang,[2,3] and Gaorong Han[2,*]

[1]*Departments of Aerospace Engineering, Mechanical Engineering and Material Science and Engineering,*
Iowa State University, Ames, Iowa 50011, USA
[2]*State Key Laboratory of Silicon Materials, Department of Materials Science and Engineering, Cyrus Tang Centre*
for Sensor Materials and Applications, Zhejiang University, Hangzhou 310027, People's Republic of China
[3]*Center of Electron Microscope of Zhejiang University, Hangzhou 310027, People's Republic of China*

A mechanism for crystal-crystal phase transformations (PTs) via surface-induced virtual premelting is justified thermodynamically and confirmed experimentally for the PTs in $PbTiO_3$ nanofibers. When the thickness of the surface melt (which appears much below the melting temperature, especially for nano-objects) exceeds the size of the critical product nucleus, nucleation and growth of the product crystal occur. For nanowires, premelting starts near the smallest size, and hydrodynamic flow driven by reduction in the external surface leads to a large change in shape and further promotion of crystal-crystal PT. During the product crystal-growth stage, virtual melting is observed experimentally within the crystal-crystal interface.

Numerous reconstructive phase transformations (PTs) between two crystal lattices lead to a high-energy semicoherent or incoherent interfaces.[1] In addition, changes in the volume and shape of the lattice result in the appearance of large internal stresses, the elastic energy of which further reduces the driving force for PTs.[1–3] This leads to suppression of nucleation and growth of the product phase, keeping the parent phase in a metastable state far from equilibrium. Plasticity can relax elastic stresses, but it is usually suppressed at a nanometer scale because of a lack of dislocations and dislocation sources. In previous work,[4–6] virtual melting (VM) was suggested as a possible mechanism of internal stress relaxation during crystal-crystal and crystal-amorphous PTs. Thus, fluctuational crystal-crystal PT generated huge amounts of energy of internal stresses, which effectively reduced the melting temperature T_m and caused melting significantly below T_m. Stress relaxation due to melting brought the melt to a highly unstable state below T_m and led to solidification to either amorphous or stable crystalline phases, completing PT. Alternatively, PT via VM was caused by a specific pressure-temperature phase diagram, in which melting temperature was reduced with the growing pressure.[6] The VM was found to be a part of sublimation within elastoplastic material.[7] While there are multiple indirect supports for the PTs via VM,[4–8] direct confirmation is still lacking. Irrespective of solid-solid PTs and VM,[4–7] reduction in surface energy during melting causes surface premelting essentially below T_m.[9–13] In addition, for nano-sized particles T_m are further reduced due to the increased contribution from the surface.[10–12]

Here, we justify thermodynamically and confirm experimentally a mechanism for crystal-crystal PT via surface-induced virtual premelting. Surface premelting of the parent phase 1 starts below its melting temperature, T_{m1}, and the thickness l_m of the thermodynamically equilibrium molten layer increases with increasing temperature. When l_m exceeds the size of the critical nucleus of the product phase 2, melt becomes unstable with respect to phase 2, and multiple nucleation and growth of phase 2 occurs. If the melting temperature T_{m2} of phase 2 is much higher than the temperature T of the experiments, melt may be completely unstable with

respect to phase 2 and represent a short-lived intermediate state in PT $1 \rightarrow 2$. That is why we call this process the surface-induced virtual premelting. For nanoparticles, further reduction in surface premelting and, consequently, PT $1 \rightarrow 2$ temperature follows from thermodynamics. For nano-objects with multiple geometric sizes (e.g., nanofibers), premelting starts near the smallest size. An additional phenomenon, driven by a reduction in surface energy and external surface, is the hydrodynamic flow along the surface that leads to large reshaping toward equaling sizes of a nano-object. Thus, nanofibers with cubic lattices tend toward nanocubes with rounded edges and corners. Surface flow increases the thickness of melt near large-size faces, thus further promoting crystal-crystal PT via surface premelting. If the energy of the crystal-crystal interface is larger than the energy of two crystal-melt interfaces, VM will be present within a propagating crystal-crystal interface. Theoretical predictions are confirmed experimentally for the PT from recently synthesized metastable, tetragonal preperovskite (PP)[14,15] to cubic perovskite (CP) in $PbTiO_3$ nanofibers—an important ferroelectric material. Thus, surface melting and large reshaping of long nanofibers into cubes with rounded faces, edges, and corners due to hydrodynamic flow are recorded *in situ* using transmission electron microscopy (TEM) in the temperature range of 823–923 K. High-resolution TEM (HRTEM) on the quenched sample confirmed that all PP and perovskite phases are separated by highly disordered interphases, which is consistent with quenched VM. The observed mixture of nanocrystalline and amorphous phases is consistent with multiple nucleation within the molten layer. The observed VM mechanism is very unexpected because it occurs much below the melting temperature, 1554 K, of the product CP phase.

Let us consider reconstructive crystal $1 \rightarrow$ crystal 2 PT with large volumetric transformation strain ε_0. The energy of the surface layer of phase 2 on the plane face of phase 1 per unit area is [9,16,17]

$$E_{12} = \gamma_2 + \gamma_{12} + (F_2 + g_e - F_1)l_2 + \Delta\gamma_{1-2}\exp(-l_2/\delta_{12}),$$

$$(1)$$

where l_2 is the thickness of the layer, δ_{12} is proportional to the width of the 1-2 interface, F is the bulk thermal free energy, $g_e \geqslant 0$ is the elastic energy due to ε_0, and $\Delta\gamma_{1-2} = \gamma_1 - \gamma_2 - \gamma_{12}$ is the change in surface energy during PT 1-2, with γ_1, γ_2, and γ_{12} for phase 1-vapor, phase 2-vapor, and phases 1-2 interface energies, respectively. The last term with thickness-dependent interfacial energy appears for small thickness l_2 of the layer 2 and takes into account the interaction of the interfaces (in the given case, phases 1-2 and 2-vapor interfaces). Here and below, we use for simplicity the exponentially decayed interaction between interfaces, corresponding to the short-range interaction. While in real systems various other types of interactions between interfaces (for example, long-range dispersion interaction) and their descriptions are used as well,[16,17] qualitatively none of our results will not change if these additional interactions are taken into account. Let $\Delta\gamma_{1-2} < 0$ because of large phase 1-2 interface energy γ_{12}. Then, since energy increases for small l_2, barrierless nucleation of phase 2 is impossible. Also, while the system is in the region of stability of phase 2 ($F_1 > F_2$), because of large ε_0 and consequently g_e, the bulk driving force $F_1 - F_2 - g_e$ is small or even negative. That is why thermally activated surface nucleation of phase 2 or nucleation of phase 2 inside of phase 1 (which is treated, for example, in Refs. 1 and 6) is impossible during the time of the experiment.

Similarly, the energy for surface premelting of the plane face of phase 1 [Fig. 1(a)] is

$$E_{1m} = \gamma_m + \gamma_{m1} + (F_m - F_1)l_m + \Delta\gamma_{1-m}\exp(-l_m/\delta_{m1}),$$
$$(2)$$

where $\Delta\gamma_{1-m} = \gamma_1 - \gamma_m - \gamma_{m1}$ and δ_{m1} is proportional to the width of the solid-melt interface.[8] Since for premelting $T < T_{m1}$, then $F_m > F_1$. For $\Delta\gamma_{1-m} > 0$ (i.e., when the total surface energy reduces during premelting), energy reduces for small l_m, and barrierless melt nucleation occurs. Minimization of the energy with respect to l_m results in equilibrium thickness of the surface layer:

$$l_m^e = \delta_{m1}\ln[\Delta\gamma_{1-m}/(F_m - F_1)\delta_{m1}]. \quad (3)$$

We consider the case with $T_{m2} \gg T_{m1}$. Thus, while surface melt is in equilibrium with phase 1, it is strongly unstable with respect to phase 2, and critical nuclei of stable phase 2 may appear inside the molten layer [Fig. 1(a)]. For a spherical nucleus, the kinetic nucleation criterion, $G_{cr} = 16\pi\gamma_{m2}^3/$
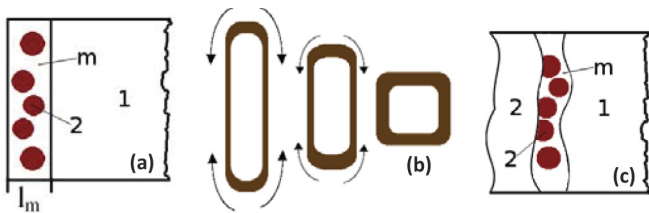

FIG. 1. (Color online) (a) Scheme of barrierless nucleation of the molten layer at the surface of phase 1 followed by thermally activated nucleation of phase 2 inside the surface melt. (b) The hydrodynamic flow of a surface melt along the surfaces, driven by decreases in the surface area and energy. (c) Melting at the propagating or stationary phase 1-2 interface followed by thermally activated nucleation of phase 2 inside the melt.

$3(F_m - F_2)^2 = 40kT$ (Ref. 1), where G_{cr} is the energy of the critical nucleus and k is the Boltzmann constant, can be easily satisfied because of $\gamma_{m2} \ll \gamma_{12}$ and large $F_m - F_2$. In addition, the diameter of the critical nucleus $d_{cr} = 4\gamma_{m2}/(F_m - F_2)$ should be smaller than l_m. Thus, under the conditions defined above, when *direct PT crystal 1$\rightarrow$2 is impossible*, it may occur via surface-induced virtual premelting at a temperature below T_{m1} and much below T_{m2}. Since with the decrease in the particle radius the thickness of the premolten layer increases and melt spreads through the entire particle at a lower temperature,[10,11] PT 1 $\rightarrow$ 2 via surface-induced virtual premelting can occur at even lower temperatures in nanoparticles.

Let us consider a nanofiber [Fig. 1(b)] with a square cross section. Since T_m reduces with the increasing of the curvature,[10,11] premelting starts at the corners, the edges, and the smallest side of the nanofiber. Since reduction in surface area reduces total energy of the system and surface energy melt-vapor is isotropic, there is a thermodynamic driving force to round corners and edges and to change the entire shape toward equal sizes and spherical shape. Such a tendency can be realized through the hydrodynamic flow of a premelt along the surfaces. The most important is the flow from the smallest faces of a nanofiber toward larger faces [Fig. 1(b)]. Removal of melt from the smallest faces causes further melting up to l_m^e; i.e., this process is self-supporting. Increasing melt thickness at large faces due to melt arrival increases the tendency to solidification, either to phase 1 (down to l_m^e) or to phase 2, because of the reducing constraint on the size of the critical nucleus. Hydrodynamic flow and reshaping will occur until the crystal reaches a stationary state. If, at the given temperature, the thickness of the molten layer is small with respect to crystal size, the stationary state will represent a cube with rounded faces, edges, and corners. The larger the thickness of the molten layer, the more close the stationary state to a sphere will be. The hydrodynamic flow competes with the crystallization process. For very fast crystallization in the molten layer, flow will be completely suppressed; for slow crystallization, it may be profound. Since crystallization is stochastic, as well as the initial shape and size of crystals, one would expect an entire range of changes in shape, from practically unchanged to close to cubic or spherical.

Next, we analyze the thermodynamics of melting within the propagating or stationary 1-2 interface [Fig. 1(c)]. The energy is

$$E_{1m2} = \gamma_{m2} + \gamma_{m1} + (F_m - F_1 - g_e)l_m + \Delta\gamma\exp(-l_m/\delta_{m1}),$$
$$(4)$$

where $\Delta\gamma = \gamma_{12} - \gamma_{m2} - \gamma_{m1}$ and it is taken into account that higher-energy phase 1 melts and complete relaxation of internal stresses occurs. For the high-energy 1-2 interface, $\gamma_{12} > \gamma_{m2} + \gamma_{m1}$, which leads to a barrierless appearance (below T_{m1}) of the molten layer of the equilibrium width,

$$l_m^e = \delta_{m1}\ln[\Delta\gamma/(F_m - F_1 - g_e)\delta_{m1}]. \quad (5)$$

Such a melting is similar to some extent to the melting in the grain boundary and the existence of equilibrium quasiliquid thin layers within various interfaces;[16–20] however, there are important differences. Since in our case interface propagates, melting at each material point represents an intermediate state

along the transformation path between phases 1 and 2; i.e., it represents VM. In addition, it is promoted by relaxation of elastic stresses and melt is not in equilibrium with contacting phases. If the width of the molten layer exceeds the size of the critical nucleus of phase 2, multiple nucleation of phase 2 will occur simultaneously with translational motion of the 1-VM-2 interface. This leads to morphological instability of the plane interface and multiple nanograin microstructures [Fig. 1(c)]. The above analysis also implies that, after critical nuclei of phase 2 appear and grow within the premolten surface layer, they do not produce phase 1-2 interfaces with the preexisting phase 1; phases 1 and 2 are separated by a molten layer. Since grains have stochastic orientation, multiple disordered grain boundaries appear, leading to a mixture of nanocrystalline and disordered phases. After holding long enough at high temperature, the system tends to transform to a large-grain and single-crystal structure through migration of the grain boundaries, thus reducing the total energy. Note that the same processes should occur inside of the premolten surface layer. An analysis for the propagating interface developed here essentially differs from that in Refs. 4–6, where the changes in the surface energy, nucleation, and morphological instability were neglected and thermal fluctuations were required.

We have found *experimental evidence* for PT in PbTiO$_3$, a prototypical ferroelectric with perovskite-type structure, which has been intensively explored in terms of its ferroelectricity and PT.[21,22] In contrast to all known perovskite phases that are characterized by a three-dimensional (3D) network of corner-sharing TiO$_6$ octahedra with a transition metal ion at the center, recently a tetragonal PP PbTiO$_3$ nanofiber has

been synthesized by our group, which is characterized by a 1D columned structure with edge-shared TiO$_6$ octahedron pairs stacking over adjacent pairs in an interlaced manner along the c axis.[14] This 1D structured PbTiO$_3$ adopts the same molecular formula and composition as those of perovskite PbTiO$_3$.[14] Here, we report PP-CP single-crystal PT via surface-induced virtual premelting after air annealing treatment in the temperature range 823–923 K. After cooling to room temperature, CP transforms to stable tetragonal perovskite (TP), which is not studied here in detail. All PTs are confirmed using *in situ* x-ray diffraction (XRD) (Fig. S1).[23] The volumetric strain for PP-CP PT is $\varepsilon_0 = -0.144$, which is large and suppresses direct PP-CP transformation because of large elastic energy. Figure 2(a) shows a large change in the shape of a nanofiber from prismatic to cubic with rounded corners, edges, and faces during PP-CP PT at $T = 873$ K within 164 s (Movie S1 and Fig. S2).[23] Figures 2(b)–2(i) reveal the change of PP to corrugated TP nanofibers, as well as rounding of the cross section of nanofiber after PT PP-CP, and then to TP perovskite. Different degrees of the change in shape were observed for different fibers, from almost undetectable to the large, as in Fig. 2(a). The only way to explain such a change in morphology is by assuming the surface premelting and hydrodynamic flow along the surface, as described above. The only alternative may be a surface diffusion.[24] However, there is no driving force for diffusion toward corrugated structure, which can only be obtained when surface flow is interrupted by contact with other nanofibers. Also, diffusion does not explain the huge scatter in the degree of reshaping. To promote diffusion, a 1-h heating treatment of the PP phase
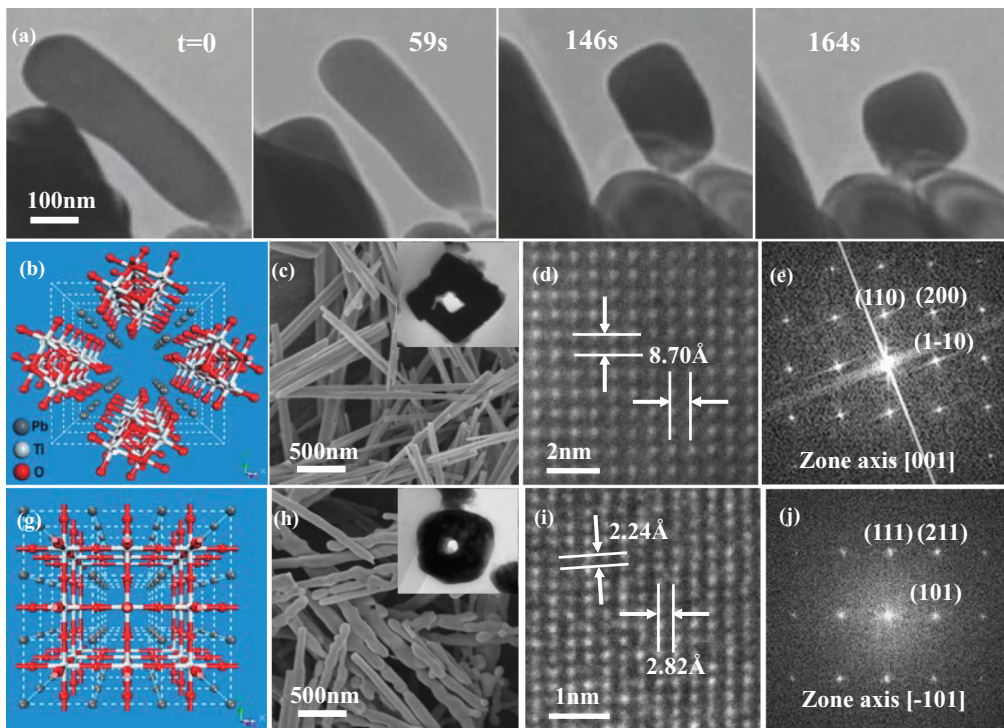

FIG. 2. (Color online) (a) Large change in shape of nanofiber from prismatic to cubic during PP-CP PT at $T = 873$ K within 164 s. (b)–(i) Change in crystal structure, morphology, and lattice images between two PbTiO$_3$ nanofibers after annealing of the PP nanofiber in air at 923 K for 30 min and cooling to room temperature. (b)–(e) PP. (f)–(i) TP. Insets in panels (c) and (h) indicate the cross-section TEM images corresponding to PP and TP PbTiO$_3$ nanofibers of ~150 nm, respectively.
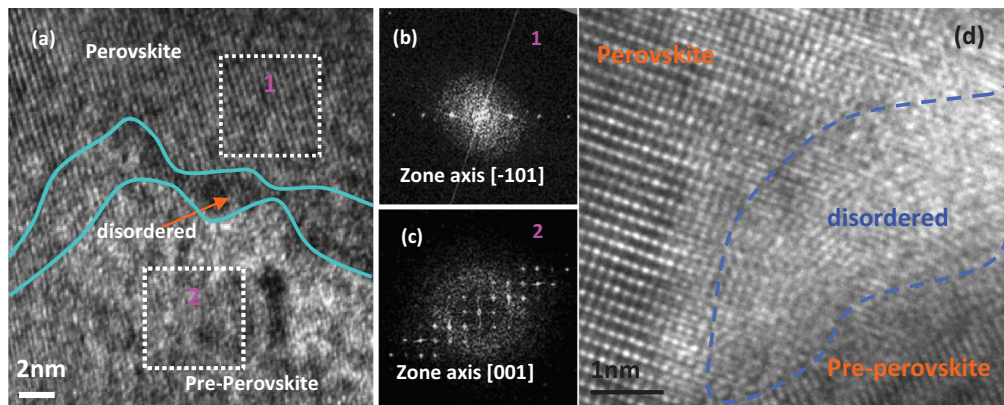
FIG. 3. (Color online) (a) HRTEM image of PP and tetragonal perovskite $PbTiO_3$ regions and interface between them quenched after treatment at $T = 923$ K for 10 min. (b) and (c) Corresponding selected area electron diffraction (SAED) patterns obtained by Fourier transformation of areas 1 and 2 in panel (c). (d) An enlarged HRTEM image of cross section of the $PbTiO_3$ nanofiber clearly demonstrates the coexistence of perovskite and pre-perovskite phases separated by a highly disordered region. The SEM image of the sample is presented in Fig. S5b.[23] The region with the mixture of highly disordered and nanocrystalline material of a width of 1 to 4 nm is observed at the interface between the two phases [see panels (a) and (d)], which is consistent with quenched VM.

nanofibers at 923 K was performed, which after annealing led to the TP phase (Fig. S3).[23] Only a few fibers were transformed to cubiclike nanocrystals, while most of the fibers kept the 1D shape (Fig. S5b).[23] Also, the PP nanofibers were heated at 1073 K for 5 min and cooled quickly to room temperature. The sample almost completely transformed to perovskite $PbTiO_3$ (Fig. S4),[23] but the change in geometry was small (Fig. S5d).[23] Thus, diffusion cannot be responsible for the large change in shape. The hydrodynamic flow of the premelted layer competing with stochastic crystallization can explain the variety of changes in shapes. The results also imply that for PP $T_m > 1073$ K.

HRTEM on the quenched sample (Fig. 3) revealed that all PP and TP phases are separated by regions with a mixture of highly disordered and nanocrystalline material, which is consistent with quenched VM. The irregular geometry of an interface is consistent with multiple morphological instabilities because of multiple nucleations under highly nonequilibrium conditions within VM.

To summarize, all of our thermodynamic predictions for a mechanism for crystal-crystal PT via surface-induced virtual premelting are confirmed from the above experiments. This includes formation of the molten phase at the surface much be-

low melting temperature, hydrodynamic flow along the surface that competes with crystallization and leads to various (from invisible to very large) changes in the crystal's shape toward equilibrium shape, the presence of the highly disordered region of the width of 1–4 nm within the PP-TP interface, and a mixture of highly disordered and nanocrystalline phases that evolve in time to a highly ordered single crystal. Such an experimental confirmation increases the plausibility of other VM-related PT mechanisms.[4–6] By changing the surroundings, one can control the surface energy and consequently the thermodynamics, kinetics, and mechanisms of such PTs. This work also has provided a way to reduce transformation temperature for solid-solid PT. A transformation mechanism can be tailored for other material systems, leading to nanomaterials adopting different crystal structures, which may be useful for mechanical and electronic nanodevice applications.

*To whom correspondence should be addressed: vlevitas@iastate.edu and hgr@zju.edu.cn

[1] D. A. Porter and K. E. Easterling, *Phase Transformation in Metals and Alloys* (Van Nostrand Reinhold, New York, 1992).

[2] F. C. Larché and J. W. Cahn, Acta Metall. **33**, 331 (1985).

[3] M. A. Grinfeld, *Thermodynamic Methods in the Theory of Heterogeneous Systems* (Longman, London, 1991); Dokl. Akad. Nauk SSSR **251**, 10 (1980).

[4] V. I. Levitas, B. F. Henson, L. B. Smilowitz, and B. W. Asay, Phys. Rev. Lett. **92**, 235702 (2004).

[5] V. I. Levitas, B. F. Henson, L. Smilowitz, and B. W. Asay, J. Phys. Chem. B **110**, 10105 (2006).

[6] V. I. Levitas, Phys. Rev. Lett. **95**, 075701 (2005).

[7] V. I. Levitas and N. Altukhova, Phys. Rev. B **79**, 212101 (2009).

[8] S. L. Randzio and A. Kutner, J. Phys. Chem. B **112**, 1435 (2008).

[9] J. F. Van der Veen, Surf. Sci. **433**, 1 (1999).

[10] J. W. Cahn, J. G. Dash, and H. Y. Fu, J. Cryst. Growth **123**, 101 (1992).

[11] V. I. Levitas and K. Samani, Nat. Commun. **2**, 284 (2011).

[12] P. R. Couchman and W. A. Jesser, Nature (London) **269**, 481 (1977).

[13] F. Delogu, J. Mater. Sci. **43**, 2611 (2008).

[14] Z. H. Ren *et al.*, J. Am. Chem. Soc. **132**, 5572 (2010).

[15] L. H. Ni *et al.*, J. Appl. Phys. **110**, 063506 (2011).

[16] J. Luo, Crit. Rev. Solid State Mater. Sci. **32**, 67 (2007).

[17] J. Luo and Y. M. Chiang, Annu. Rev. Mater. Res. **38**, 227 (2008).

[18] A. M. Alsayed, M. F. Islam, J. Zhang, P. J. Collings, and A. G. Yodh, Science **309**, 1207 (2005).

[19] R. Kikuchi and J. W. Cahn, Phys. Rev B **21**, 1893 (1980).

[20] M. Baram, D. Dominique Chatain, and W. D. Kaplan, Science **332**, 206 (2011).

[21] R. E. Cohen, Nature (London) **358**, 136 (1992).

[22] B. A. Hernandez-Sanchez *et al.*, Chem. Mater. **17**, 5909 (2005).

[23] See Supplemental Material at http://link.aps.org/supplemental/10.1103/PhysRevB.85.220104 consisting of Supplementary Movie and Supplementary Figures 1–5.

[24] Y. Khalavka, C. Ohm, L. Sun, F. Banhart, and C. Sonnichsen, J. Phys. Chem. C **111**, 12886 (2007).

Supplementary Information: Crystal-crystal phase transformation via surface-induced virtual pre-melting

Valery I Levitas[1*], Zhaohui Ren[2], Yuewu Zeng[2,3], Ze Zhang[2,3] Gaorong Han[2*]

[1]*Departments of Aerospace Engineering, Mechanical Engineering and Material Science and Engineering, Iowa State University, Ames, Iowa 50011, USA.*

[3]*State key Laboratory of Silicon Materials, Department of Materials Science and Engineering, Cyrus Tang Centre for Sensor Materials and Applications, Zhejiang University, Hangzhou 310027, P. R. China.*

[3]*Center of Electron microscope of Zhejiang University, Hangzhou 310027, P. R. China*

Movie S1. Large change in shape of the sample from rod to cube during heating at 600$^{\mathrm{o}}$C. This video was recorded about 1 min.

In-situ XRD investigation. In-situ XRD patterns of pre-perovskite PbTiO$_3$ nanofibers are shown in Fig. S1. Below 500$^{\mathrm{o}}$C, no phase transition has been observed for pre-perovskite PbTiO$_3$ nanofibers from Fig. S1a. At 550$^{\mathrm{o}}$C, obvious and new diffraction peaks grow in the XRD pattern, compared to that at 500$^{\mathrm{o}}$C, which is emphasized by a rectangular frame (dot line) in Fig. S1a. At 700$^{\mathrm{o}}$C (Fig. S1b), another phase has been obtained, which can be indexed into a conventional perovskite PbTiO$_3$ with cubic structure (a=3.97Å, space group: Pm-3m) (Glazer A.M., Mabud S.A. Powder profile refinement of lead zirconate titanate at several temperatures. II. Pure PbTiO$_3$. *Acta Cryst.* B **1978**, *34*, 1065-1070). When temperature decreasing to 25$^{\mathrm{o}}$C again (Fig. S1b), this cubic PbTiO$_3$ transforms into a typical tetragonal perovskite PbTiO$_3$ (a=3.90Å, c=4.15 Å, space group: P4mm) .
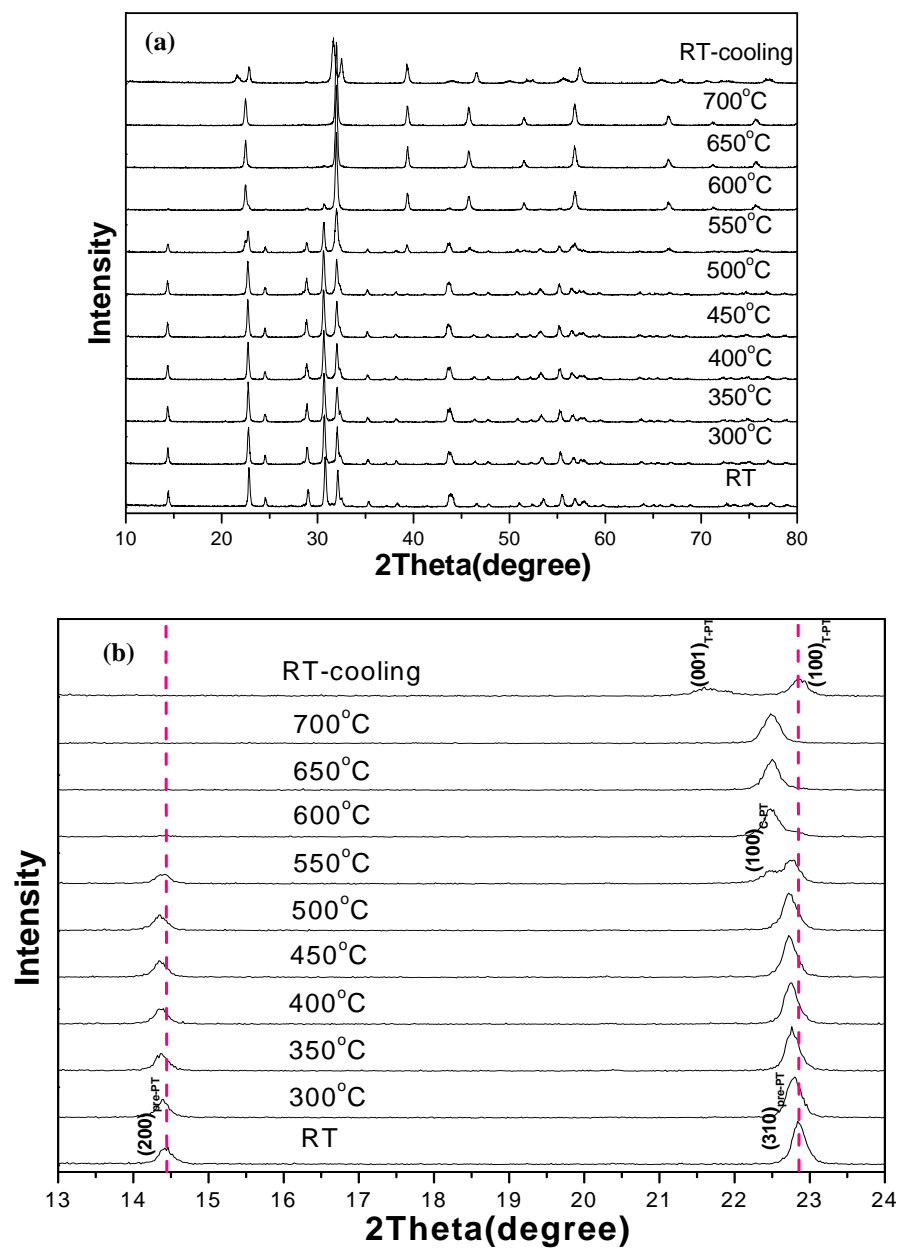
Fig. S1 (a) I*n-situ* XRD patterns of pre-perovskite PbTiO$_3$ nanofibers at different temperature. (b) Indexed XRD patterns at several temperature points deriving from Fig. S1a. *Pre-perovskite PbTiO$_3$: PP-PbTiO$_3$; Cubic perovskite PbTiO$_3$: CP-PbTiO$_3$; Tetragonal perovskite PbTiO$_3$: TP-PbTiO$_3$.*
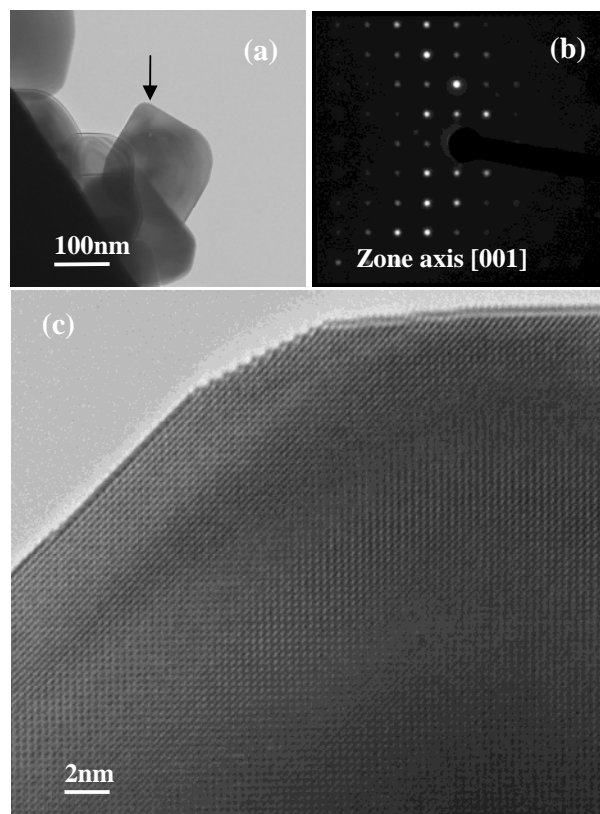
Fig. S2 *In-situ* TEM investigation of perovskite PbTiO$_3$ nanocrystals after phase transformation of pre-perovskite PbTiO$_3$ nanofibers at 600°C: (a) TEM image of perovskite PbTiO$_3$ nanocrystals; (b) and (c) Selected area electron diffraction pattern and HRTEM image of a PbTiO$_3$ nanocrystal as arrow points in Fig. S2a. These results confirm that the nanocrystals are single-crystal in nature, which can indexed into a conventional cubic structure (a=3.97Å, space group: Pm-3m) (3).
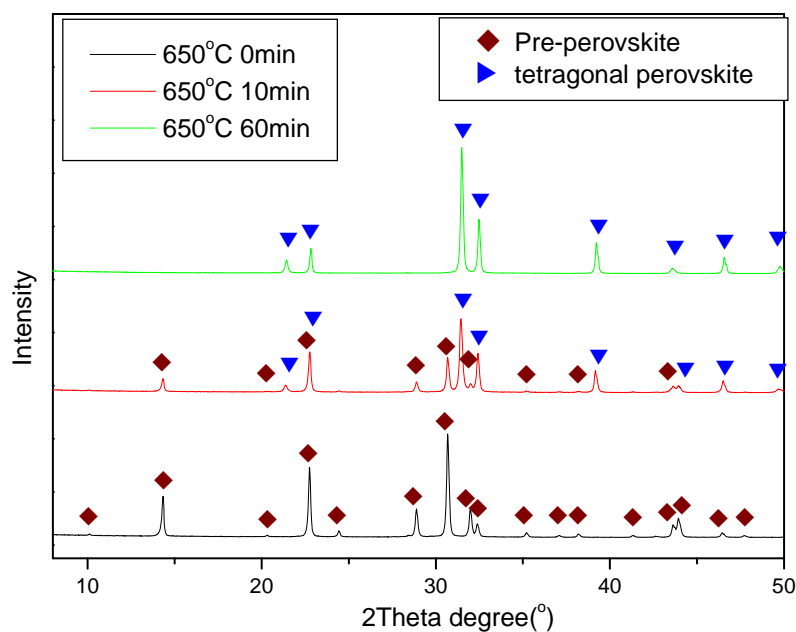
Fig. S3 XRD patterns of the pre-perovskite PbTiO₃ nanofibers after annealing in air for different time at 650°C. Note that the annealed sample for 10min at 650°C was quickly quenched to room temperature. The sample consists of PP and perovskite PbTiO₃ phase after 10min annealing and quick cooling to room temperature, while PbTiO₃ nanofibers adopt single tetragonal perovksite structure when the heating time is up to 30min and above.
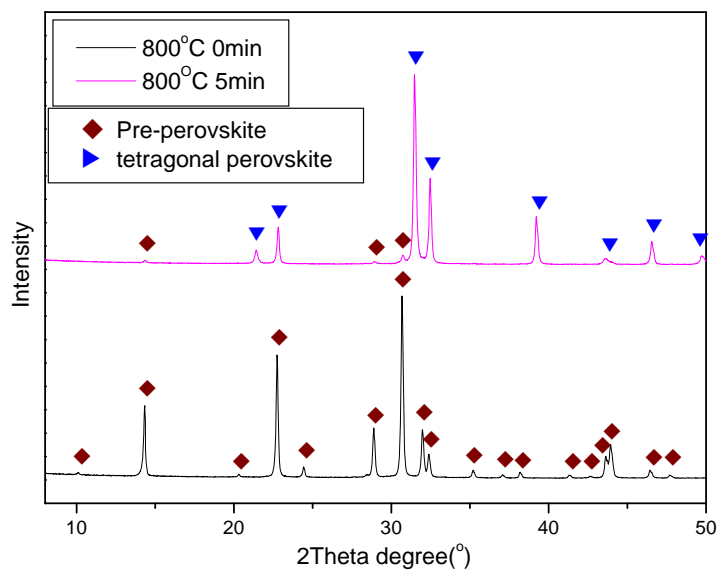
Fig. S4 XRD patterns of the pre-perovskite PbTiO$_3$ nanofibers after annealing in air for different time at 800°C. The annealed sample after 5min annealing at 800°C was quickly quenched to room temperature. After heated in air for 5min at 800°C, the PP nanofibers almost transform into perovskite ones, and in particular, the regular morphology of the nanofibers basically keep.
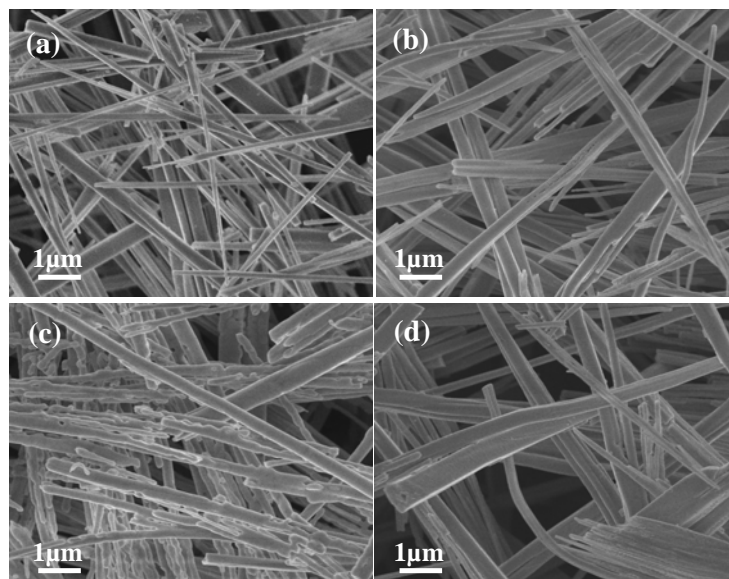
Fig. S5 SEM images of the samples prepared at different conditions: (a) as-prepared by hydrothermal method; (b) annealed in air for 10min at $650^{\circ}C$, and then quickly quenched to room temperature; (c) annealed in air for 60min at $650^{\circ}C$ and (d) annealed in air for 5min at $800^{\circ}C$, and then quickly quenched to room temperature.